CHAPTER – III

Structural, Thermal and Electrical Study of $Bi_{4-x}Me_xV_2O_{11-\delta}$ (Me=Li) Solid Solution

---

To myself I am only a child playing on the beach, while vast oceans of truth lie undiscovered before me.

Isaac Newton

3.1. Introduction

In recent times much attention has been concentrated on BIMEVOXes to introduce extrinsic vacancies so as to achieve higher oxygen ionic conductivity in these materials. The high temperature γ-polymorph can successfully be stabilized to room temperature by incorporating isovalent or aliovalent cations at the vanadium site **[1-4].** Particularly, divalent substitution for vanadium, i.e., $Bi_4V_{2-x}ME_xO_{11-\delta}$, (ME stands for divalent metals such as Cu, Co, Ti, etc.) have been widely investigated and show relatively high oxide ion conductivity in the intermediate temperature regime **[1, 2, 5].** The best ionic conductivities, known up to now, have been reported for copper, titanium and antimony members of the BIMEVOX family. On the other hand, only scanty reports are there on Bi-site substitution **[6-8].** Therefore, it is important to investigate the effect of doping at Bi-site on the phase formation and conductivity of the parent compound $Bi_4V_2O_{11}$.

A large number of investigations have been carried out on divalent doped (V-site) bismuth vanadate. However, the effect of monovalent doping has not been studied extensively **[9].** A few works have been reported on Li and Ag doping at V-site **[9-11].** In a recent brief communication, effect of Li-doping at Bi-site on the conductivity of $Bi_4V_2O_{11}$ was reported **[12].** In this chapter, we report detailed structural, thermal and electrical studies of $Bi_{4-x}Li_xV_2O_{11-\delta}$ compound with x = 0 - 0.4.

3.2 Experimental

The series of the compounds $Bi_{4-x}Li_xV_2O_{11-\delta}$ ($0 \leq x \leq 0.4$) were prepared by taking appropriate quantities of Bi_2O_3 (99%), V_2O_5 (99%) and Li_2CO_3 (99%). The details of the synthesis process have been discussed in **chapter-II**.

3.3. Results and discussion

3.3.1 X-ray diffraction

The **Fig.3.1** shows the room temperature X-ray diffraction patterns of the system $Bi_{4-x}Li_xV_2O_{11-\delta}$ ($0 \leq x \leq 0.4$). The analysis of XRD data was performed using POWD MULT Program **[13.** The experimentally observed diffraction patterns were also compared with the JCPDS ICDD (1999 version 2.02). The values of the full width half maxima (FWHM) for Williamson hall equation were evaluated using "X'pert High score plus" software. The lattice parameters were obtained considering the best agreement between observed and calculated value of interplaner spacing 'd', i.e, $\Sigma\Delta d = \Sigma(d_{obs} - d_{cal})$ = minimum.

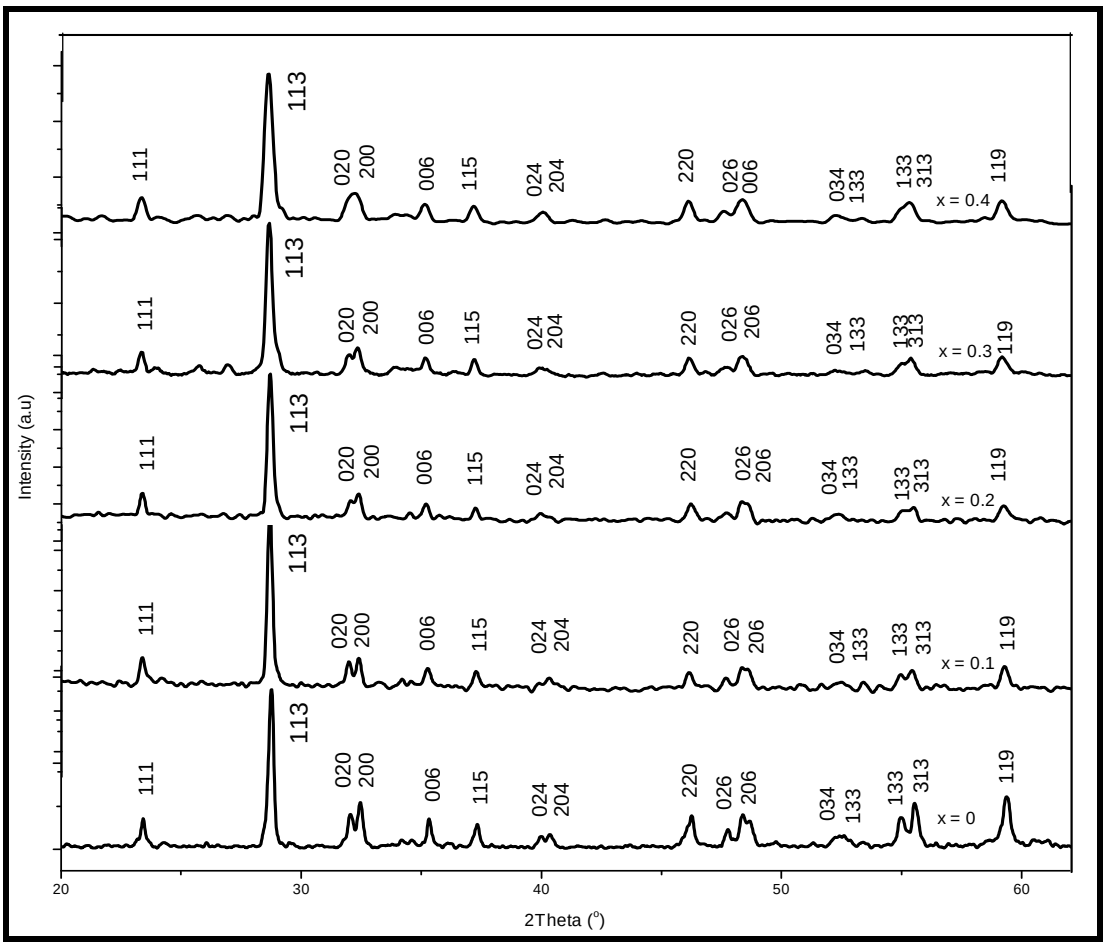

Fig. 3.1(a): XRD patterns of $Bi_{4-x}Li_xV_2O_{11-\delta}$ ($0 \leq x \leq 0.4$) compounds.

With super lattice diffraction peaks at $2\theta \approx 32^{\circ}$, 48°, and 54°, the structure of the parent compound $Bi_4V_2O_{11}$ could be indexed with α-phase of orthorhombic structure **[14-16].** Orthorhombic α-superstructure is also evident in XRD patterns of the doped composition x=0.1. For higher level of substitutions, the doublets began to converge which indicates partial suppression of orthorhombic β-polymorph at room temperature **[3].** No impurity peaks have been found to be present in the entire series of compound. The composition dependence of unit cell parameters is shown in **Table 3.1.**

Table-3.1(a): The unit cell parameters of $Bi_{4-x}Li_xV_2O_{11-\delta}$ series of compounds.

Composition	*a*(Å)	*b*(Å)	*c*(Å)	Volume(Å^3)
x = 0	5.521 (18)	5.598 (15)	15.243 (16)	471.108
x = 0.1	5.548 (12)	5.574 (09)	15.256 (11)	471.785
x = 0.2	5.556 (17)	5.568 (14)	15.286 (16)	472.884
x = 0.3	5.572 (15)	5.556 (18)	15.314 (13)	474.091
x = 0.4	5.578 (20)	5.549 (22)	15.325 (24)	474.344

For the undoped compound, the value of the lattice parameters agree with those reported earlier **[14].** It has been observed that, *b* decreases while *a* and *c* increases with increasing dopant concentration. The increase in the dimension of *c* parameter is a sign of change from α to β polymorph **[16].** A gradual increase of cell volume with x is not consistent with the substitution of larger Bi^{3+} by smaller Li^{+}**.** Considering that Li^{+} (76 pm) has smaller effective ionic radius than Bi^{3+} (103 pm), it seems that though the substitution has been done to replace Bi, it may rather substitute for V (59 pm). Moreover, the similarity between observed XRD pattern and the reported XRD pattern for Li doped at V site [16] also suggests V-site substitution of the dopent (Li). To maintain the charge neutrality either in the case of Bi-site ($Bi_{4-x}Li_xV_2O_{11-\delta}$) or V-site ($Bi_{4-x}Li_xV_{2-x}O_{11-\delta}$) substitution, the values of δ are tabulated in **Table 3.2.**

Table 3.1 (b): The value of δ corresponding to Bi/V site substitution

Composition	δ for Bi-site substitution	δ for V-site substitution
x = 0.1	0.1	0.35
x = 0.2	0.2	0.7
x = 0.3	0.3	1.05
x = 0.4	0.4	1.4

The XRD profile of all the samples shows some broadening of diffraction peaks. When the crystallite size of a material is of the order of less than 100 nm, they generally exhibit the peak broadening effect instead of sharp peaks. Another factor responsible for the XRD peak broadening may be due to lattice strain. This factor, however, in our case is not responsible for peak broadening as has been explained later in the text. Assuming that both the particle size and the strain contributed to the peak broadening effect, they can be separated by using Williamson-Hall equation, [17]

$$\beta cos\theta/\lambda = K/D + 4\varepsilon sin\theta/\lambda \quad (3.1)$$

Where, β is the full width half maxima (FWHM), D is the crystallite size, K is a shape factor (usually about 0.94), θ is the diffraction angle, ε is the strain induced and λ is the wavelength of CuK_α (λ= 1.5418 Å) radiation.

As shown in **Fig.3.1 (b)**, the size of the crystallite and the strain are calculated from the Y intercept and the slope of the graph plotted between 4 sin θ and β cos θ. The estimated crystallite sizes of the compositions lie in the range of 35nm to 54 nm and are shown in the **Fig.3.1 (b)**. For all the doped compositions, the sizes of the crystallites are found to be less than the parent compound. The microstrains induced were of the order of 10^{-4} which is very small and hence has negligible effect on XRD broadening.

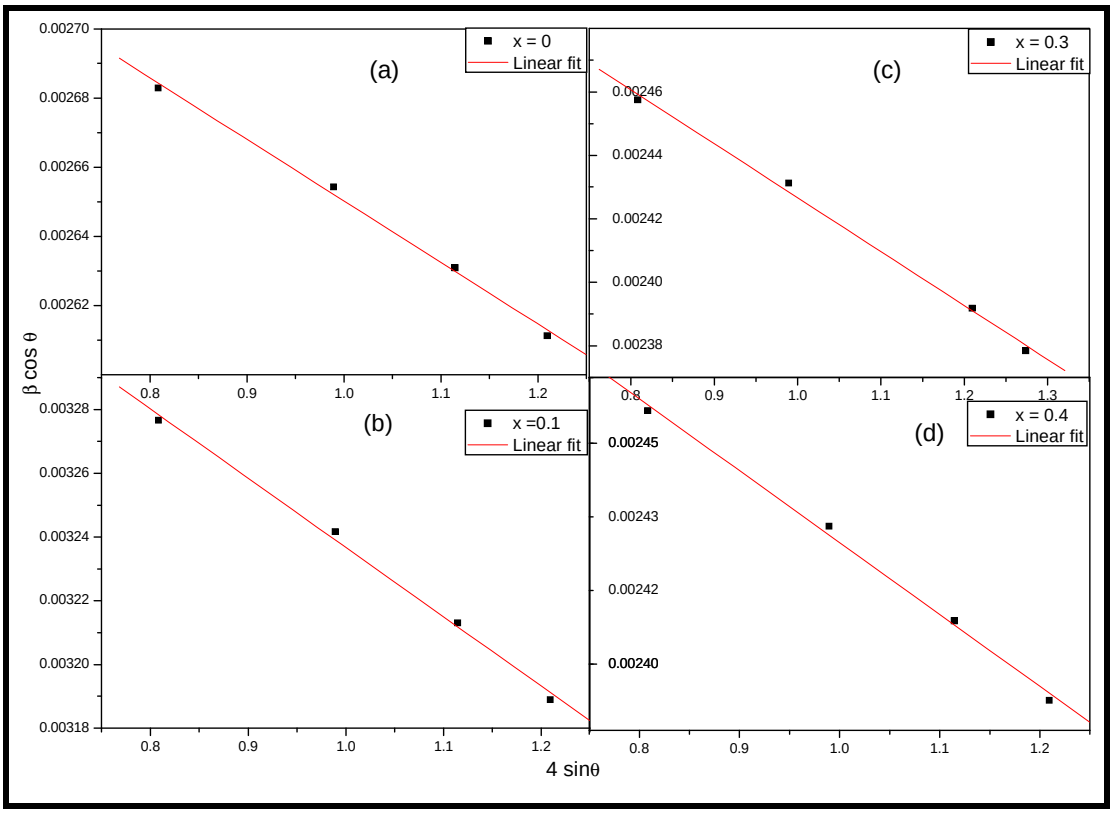

Fig. 3.1 (b): Williamson Hall plot for (a) x = 0, (b) x = 0.1, (c) x = 0.3 and (c) x = 0.4 compositions of the compound $Bi_{4-x}Li_xV_2O_{11-\delta}$.

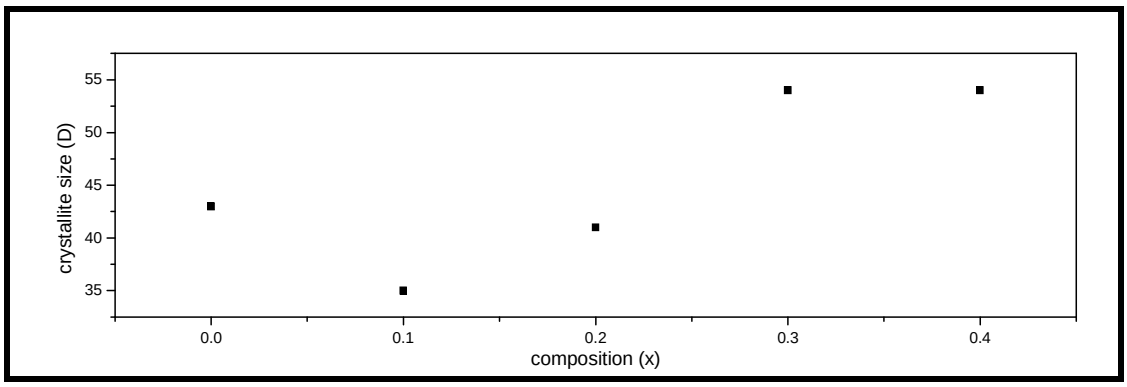

Fig. 3.1(c): crystallite size (D) Vs composition (x) of $Bi_{4-x}Li_xV_2O_{11-\delta}$ ($0 \leq x \leq 0.4$) compounds.

3.3.2. FTIR spectra

The above mentioned XRD results of $Bi_{4-x}Li_xV_2O_{11-\delta}$ system were also confirmed by FTIR spectra shown in **Fig. 3.2**. The atomic weight of Bi is 208.98 g/mol which is

much larger than that of V which is 50.94 g/mol. The atomic weight of Li is ...Moreover, the ionic radius of Bi (1.03 Å) is larger than that of V which is 0.59 Å. Thus, if Li (ionic radii) substitution takes place at at Bi-site the (Bi-O) bond length is expected to be longer and weaker compared to (V-O) bond and bringing to lower *k* value (already mentioned in **chapter II**) which may lead to lowering of υ.

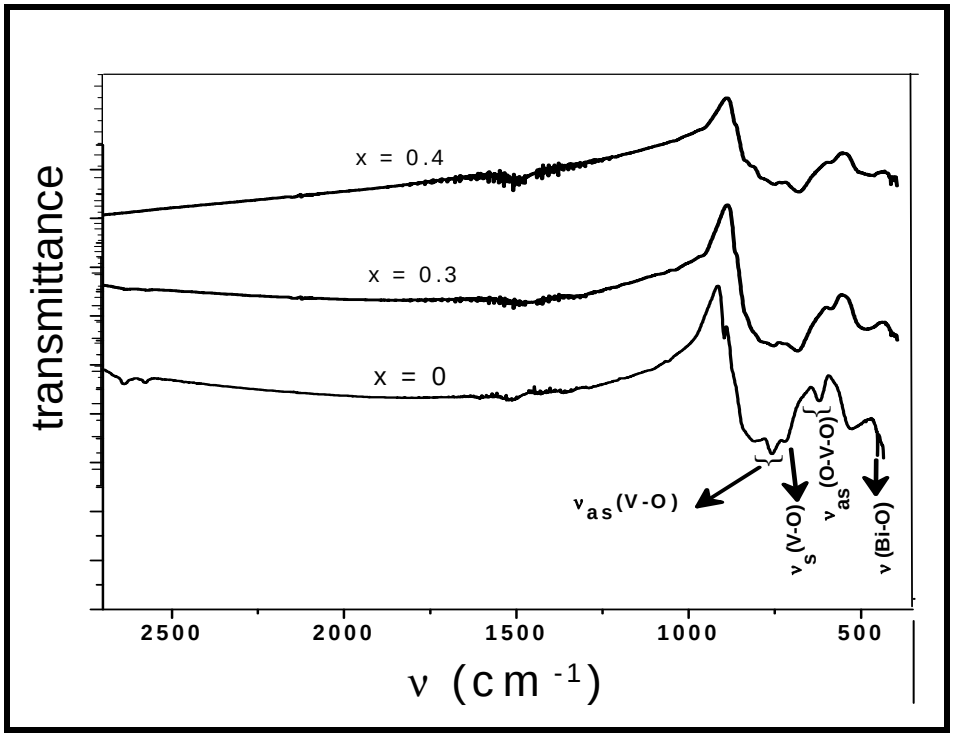

Fig.3.2: FT-IR patterns of $Bi_{4-x}Li_xV_2O_{11-\delta}$ series of compounds.

A band in the IR spectra of parent compound (x = 0) noticed at ~ 420 cm^{-1} is attributed to the symmetric stretching of (Bi-O), whereas that at ~720 is the characteristic of the symmetric stretching of (V-O) bond **[18-19].** The asymmetric stretching mode of vibration υ_{as} (V-O) and υ_{as} (O-V-O) associated with the vanadate anion present in the α- $Bi_4V_2O_{11-\delta}$ noticed at ~940 – 760 and ~660 – 500 respectively are also reported earlier in this system **[20**]. It is observed that the position of the (Bi-O) bond almost remain same. On the other hand, a gradual decrease in intensities of IR peaks and hence the fine structure is observed for the doped specimens in the region ~940 – 500 cm^{-1} which reveals crystallographic distortion in the perovskite

vanadate layer [**21**] and suggest substitution of Li at V-site for all the compositions which further supports the observations of the XRD studies (increasing cell volume with the increase Li concentration).The decreased in the IR peak intensity with increasing dopant concentration can be correlated with the partial suppression of phase transition. Hence, owing to the increased distortion in the perovskite vanadate layer the β--phase is partially suppressed for the doped composition.

3.3.3 Microstructure analysis

The scanning electron microscopy (SEM) of the fractured surfaces of the samples has been carried out to visualize the micro structural effects on the conductivity and solid solution formation (**Fig**. **3.3**). The micrographs show uniformly distributed well grown grains with good grain to grain connectivity having grain size 9-14 µm. However, few smaller grains of size 2-5 µm are formed along with the larger grains. Segregation of grains are not evident for the entire series of compound (x = 0 to x = 0.4) implying that the compounds so prepared are within the solubility limit of Li.

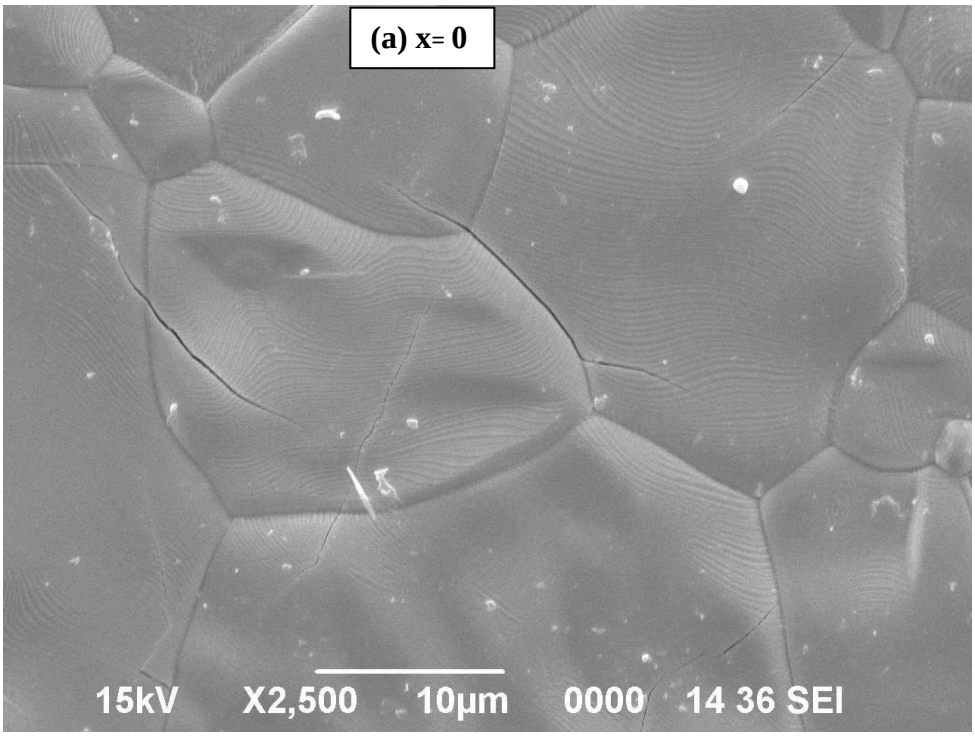

Fig. 3.3 (a): SEM image of the sintered pellet of composition x = 0

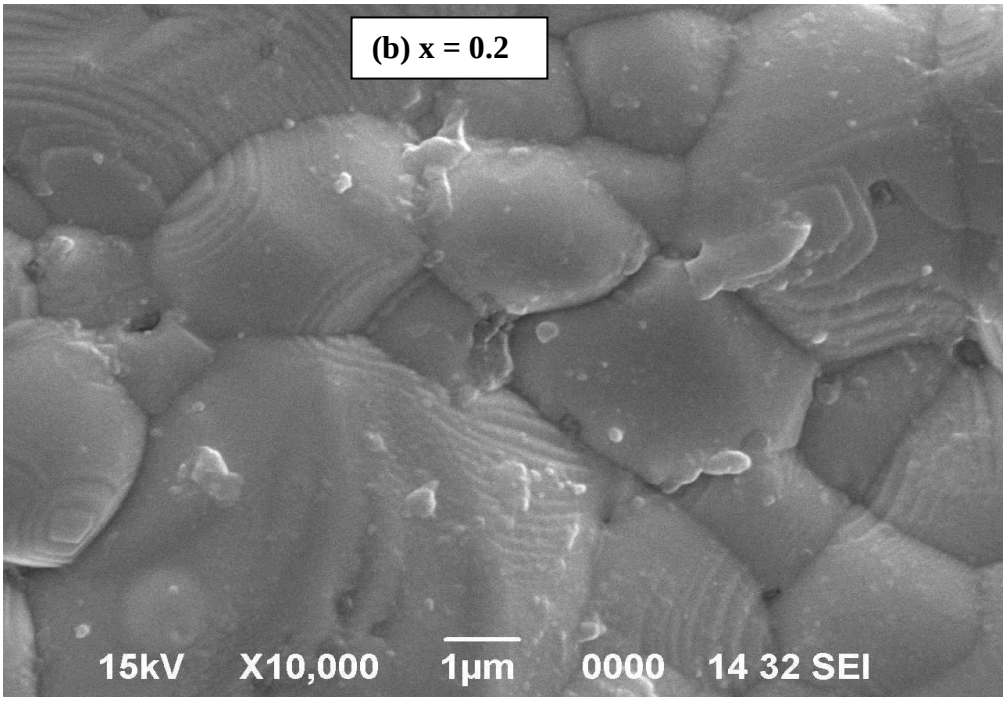

Fig. 3.3 (b): SEM image of the sintered pellet of composition x = 0.2

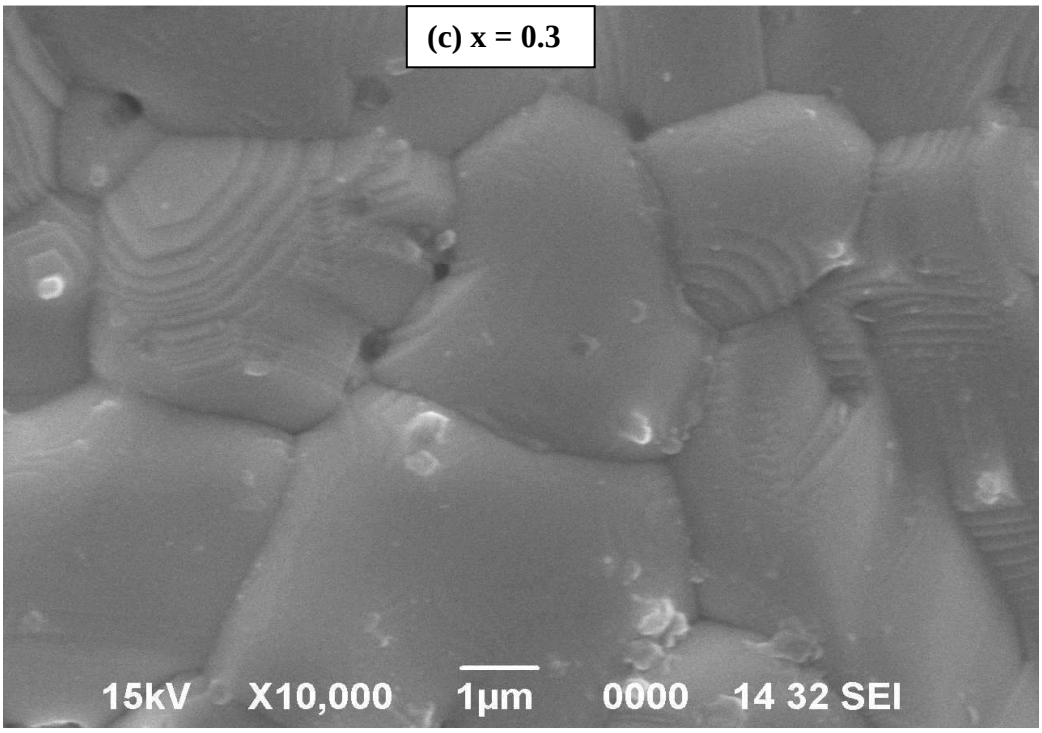

Fig. 3.3 (c): SEM image of the sintered pellet of composition x = 0.3

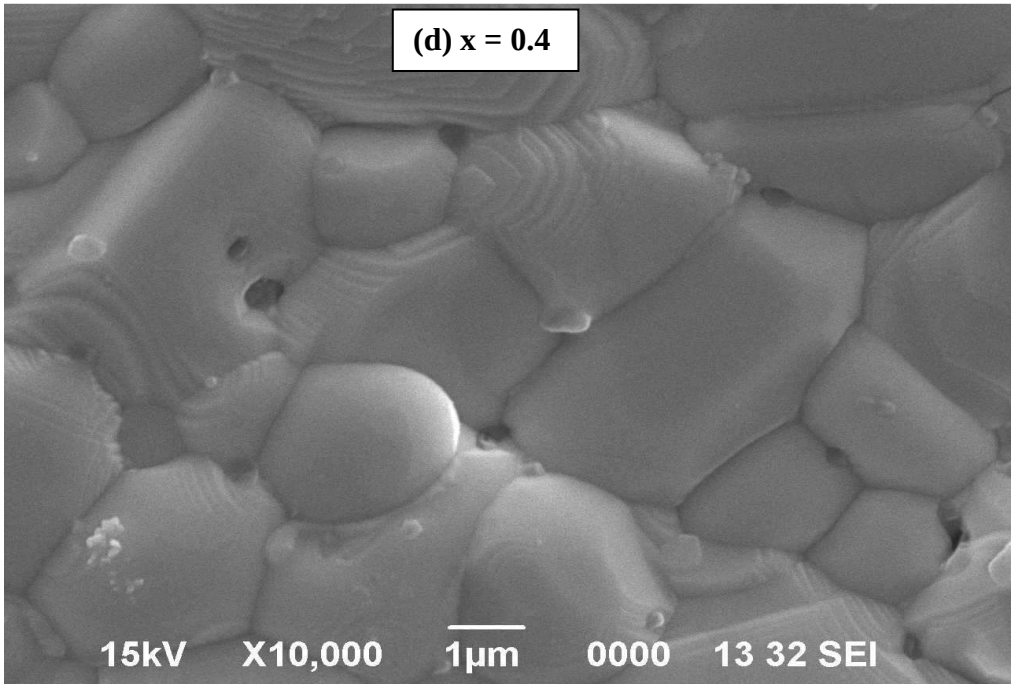

Fig. 3.3 (d): SEM image of the sintered pellet of composition x = 0.4

On careful inspection of micrographs for the samples in **Fig. 3.3**, one can see the interwoven wavy network type of structure which is more prominent for x = 0.2 and become less prominent for the compositions with higher dopant concentration. This type of wavy network structure in ceramic compounds has been observed earlier for piezoelectric materials [**23-24**]. Bismuth vanadate ($Bi_4V_2O_{11}$) has been found to be ferroelectric which belongs to the well-known ferroelectric Aurivillius family of oxides with the general formula $(Bi_2O_2)^{2+}(A_{n-1}B_nO_{3n+1})^{2-}$ [**25-27**]. During the process of sintering, the compound crystallizes (at above Curie temperature) in cubic perovskite structure and transforms in to lower symmetry structure during the process of cooling. The phase transformation results in lattice distortion which in turn generates thermal stresses. These thermal stresses are further reduced by the formation of domains. The structure comprises of these parallel domains (wavy network) formed due to the thermal lattice strain during cooling cycle of sintering process. On the other hand the gradual decrease of wavy pattern for higher level of substitutions ($x \geq 0.2$) indicates partial stabilization of β-polymorph [**28**].

3.3.4 DSC studies

DSC profiles for both heating and cooling cycles are presented in **Fig. 3.4.** In good agreement with the earlier structural observations on other BIMEVOXes, the parent as well as the doped compound show noticeable hysteresis behaviour in respect of α↔β transition which increases with x **[1, 29].** The α→β phase transition is clearly evident in the undoped as well as in the doped specimen with x = 0.1 composition. Upon heating, a strong endothermic peak for the parent compound is obtained at temperature 448 °C having enthalpy value of 8.37 J/g. Similar peak is also observed for sample with x = 0.1 composition at the same temperature but with a lower enthalpy value of 6.03 J/g indicating the beginning of suppression of α→β phase transition. In cooling cycle the corresponding peaks (exothermic) shift to 380 °C and 340 °C with respect to the compositions x=0 and x=0.1 respectively. Weak endothermic peaks around 440 °C corresponding to the compositions x= 0.3 and 0.4 with enthalpy values 1.35 J/g and 1.01 J/g are also observed in the DSC plot. Another

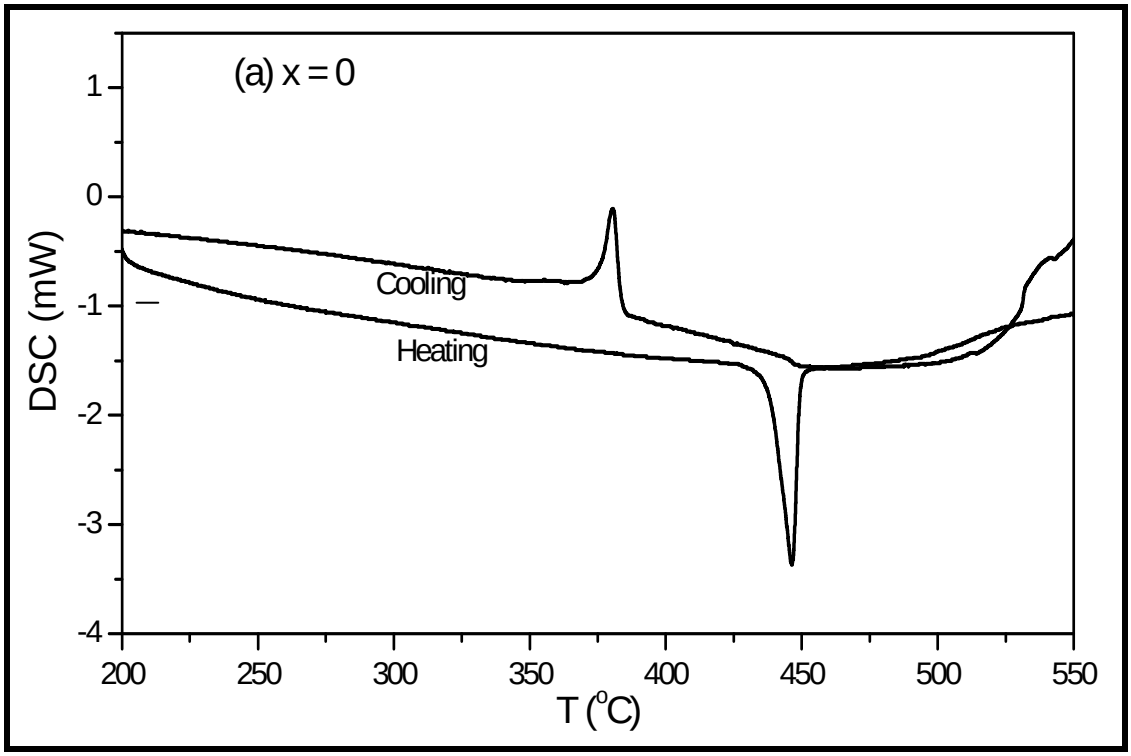

Fig. 3.4 (a): DSC profiles of $Bi_4V_2O_{11}$ compound.

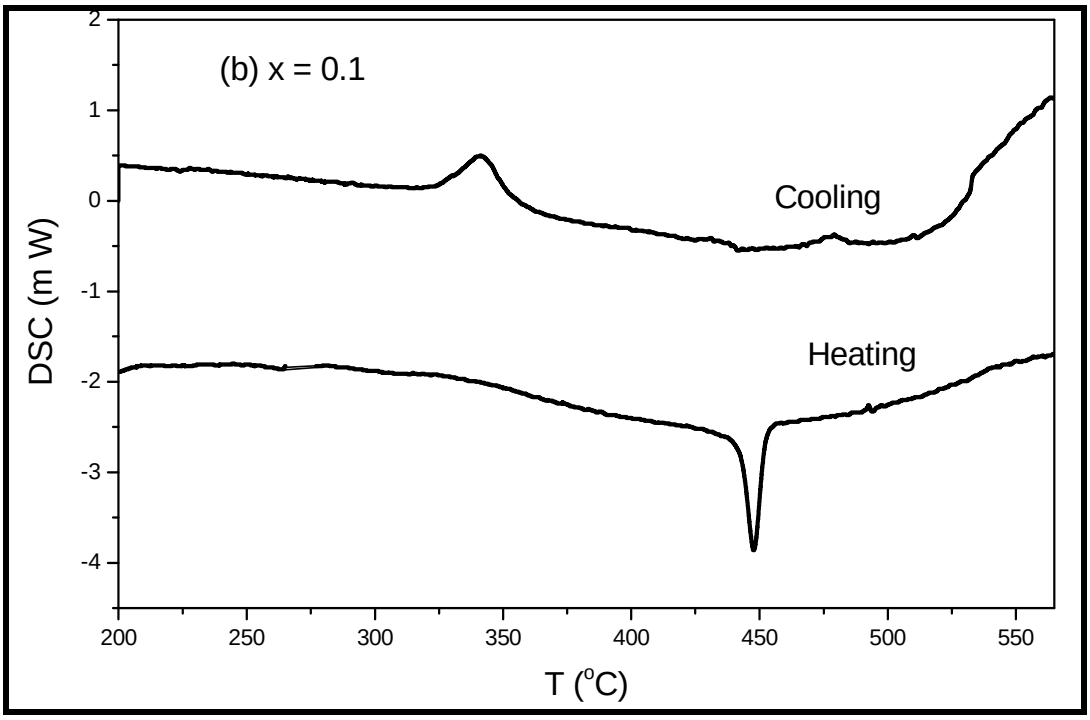

Fig. 3.4 (b): DSC profiles of $Bi_{4-x}Li_xV_2O_{11-\delta}$ (x= 0.1) compound.

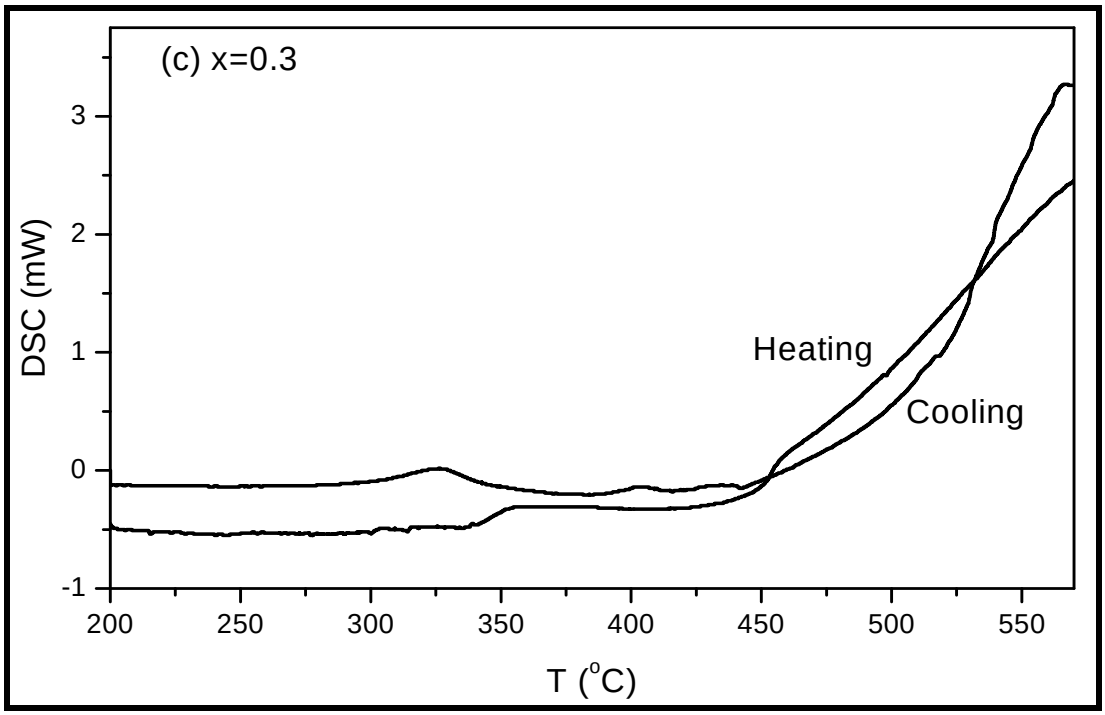

Fig. 3.4 (c): DSC profiles of $Bi_{4-x}Li_xV_2O_{11-\delta}$ (x = 0.3) compound.

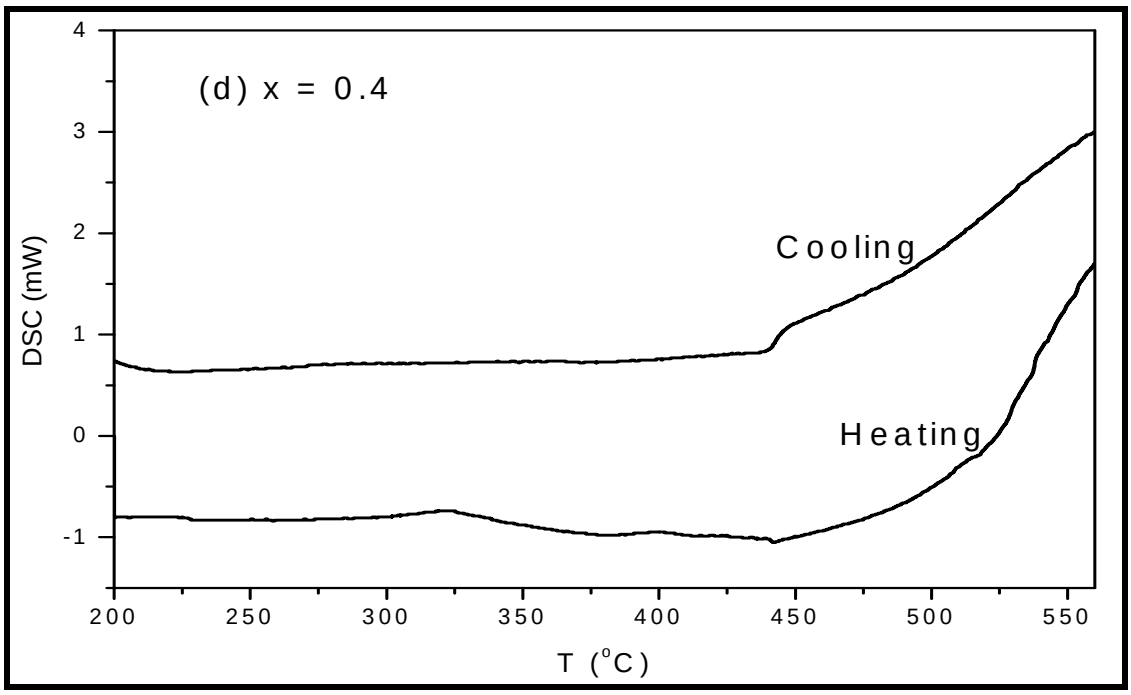

Fig. 3.4 (d): DSC profiles of $Bi_{4-x}Li_xV_2O_{11-\delta}$ (x= 0.4) compound.

endothermic peak is also visible at 550 °C for the parent compound which is an unambiguous evidence of β→γ phase transition. With the increase of dopant concentration, the peaks move towards the lower temperature with decreasing enthalpy values reveal the suppression of α→β phase change. No evidence of γ-polymorph at room temperature has been found for the entire samples of the series of compound.

3.3.5 AC impedance and conductivity analysis

The complex impedance plots of $Bi_{4-x}Li_xV_2O_{11-\delta}$ system (**Fig. 3.5**) are similar to those observed for most BIMEVOX es which exhibit two semicircular arcs at temperature below ~ 450 °C together with a low frequency spike. **Fig. 3.5 (a)** shows the impedance plane plot for the series of compounds at 300 °C. It has been observed that the overall impedance data at low temperature (300 °C) can be represented by two semicircular arcs along with an inclined spike. The high and intermediate frequency arcs of the semicircle represent the grain interior and grain boundary contributions,

respectively. The total sample resistance at different temperatures was determined from the intersection point of the semicircular arc of the spectrum at the real axis.

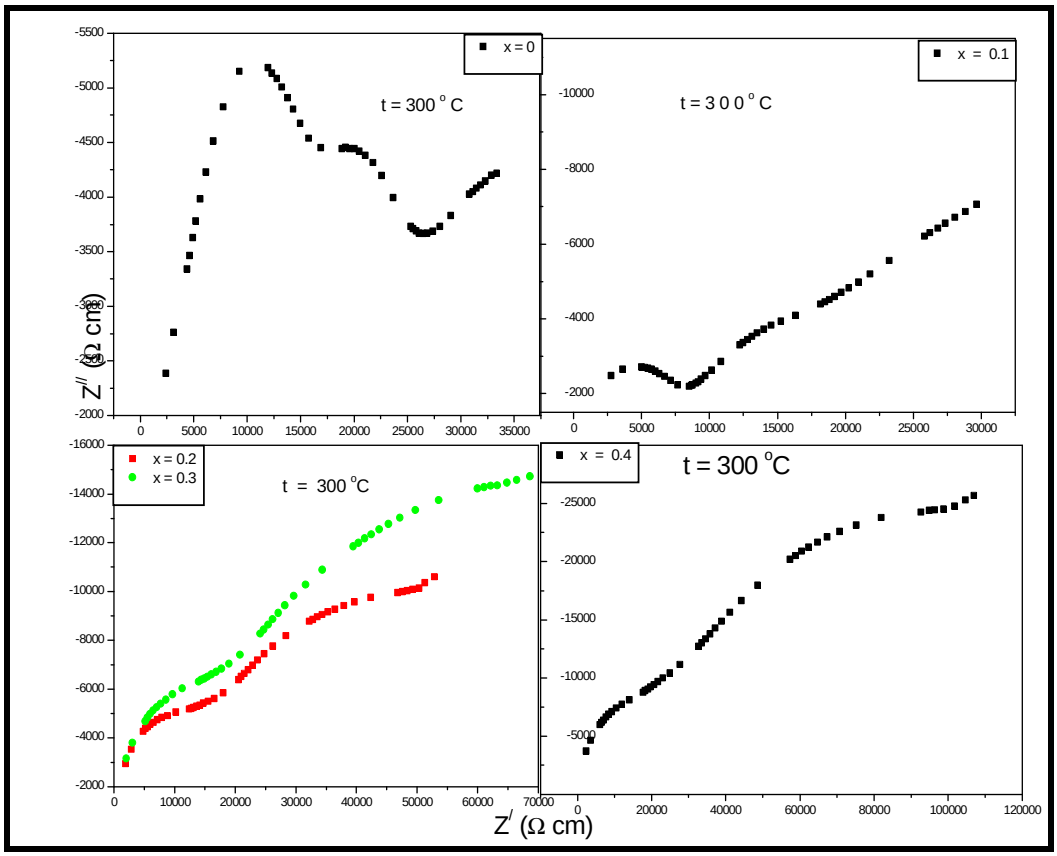

Fig. 3.5: (a) Cole-Cole plot of $Bi_{4-x}Li_xV_2O_{11-\delta}$ ($0 \leq x \leq 0.4$) at 300°C.

The grain boundary resistivity at 300 °C has been evaluated by using the geometrical parameters of the respective samples via relation S. R_{gb} /L, where S is the surface area and L is the thickness of the pellet. Though, this method of evaluation is not accurate as the actual grain boundary resistivity can only be calculated by considering the grain morphology, it may be accepted for the sake of comparison. The values of grain boundary resistivity (ρ_{gb}) for different compositions (x) at 300 °C have been shown in **Fig. 3.5 (b)**. It is evident from the figure that the grain boundary resistivity of the compounds increases with the increase of dopant concentration at 300 °C which is supported by the presence of pores in the SEM micrographs of the respective specimens.

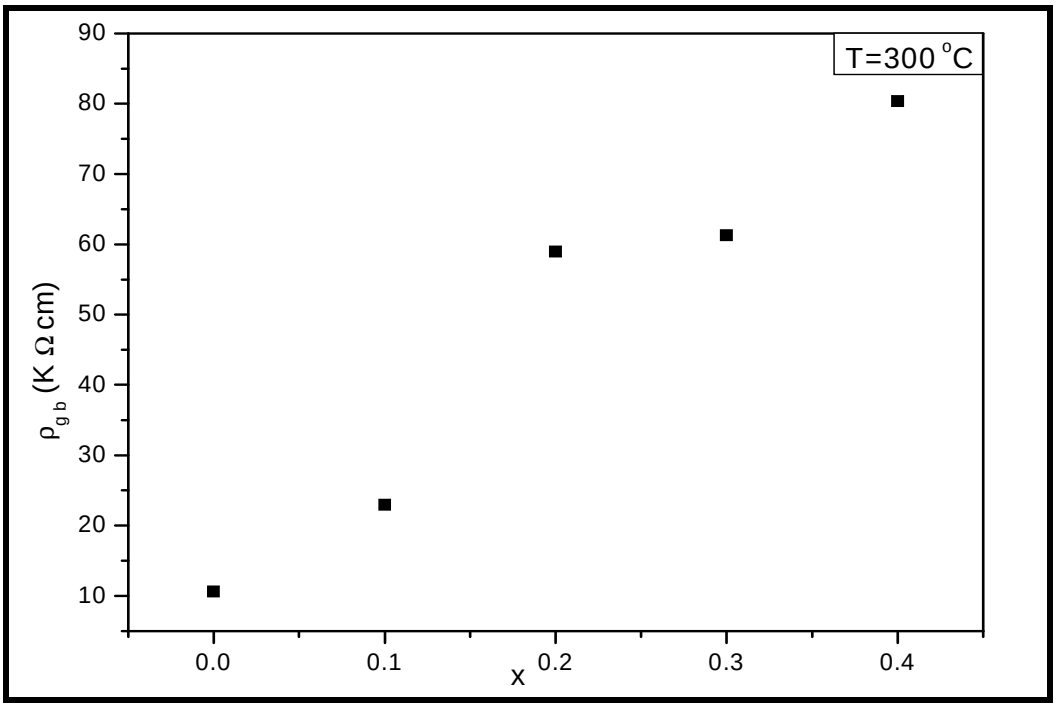

Fig.3.5 (b): Grain boundary resistivity (ρ) vs. composition (x) of $Bi_{4-x}Li_xV_2O_{11-\delta}$ ($0 \leq x \leq 0.4$) at 300 °C.

Fig. 3.5 (c) shows the impedance plane plot for the series of compounds at 500 °C. It has been observed that at higher temperatures (above ~ 500 °C), the contribution from grain boundary become negligible in all the compounds (both undoped and doped). It is clear as the two semicircles merge to a single arc together with a prominent low frequency inclined spike. The low frequency spike inclined to the horizontal is the manifestation of electrode polarization and suggest that the compound is primarily an ionic conductor **[1, 14, 16- 17].** At higher temperatures, the bulk resistivity of the undoped compound is much higher than the doped compounds. The resistivity of the doped specimens decreases gradually till x = 0.3 and again increases for x = 0.4 composition. However, the resistivity of x= 0.4 is still higher than the both undoped and the doped compound with composition x = 0.1.

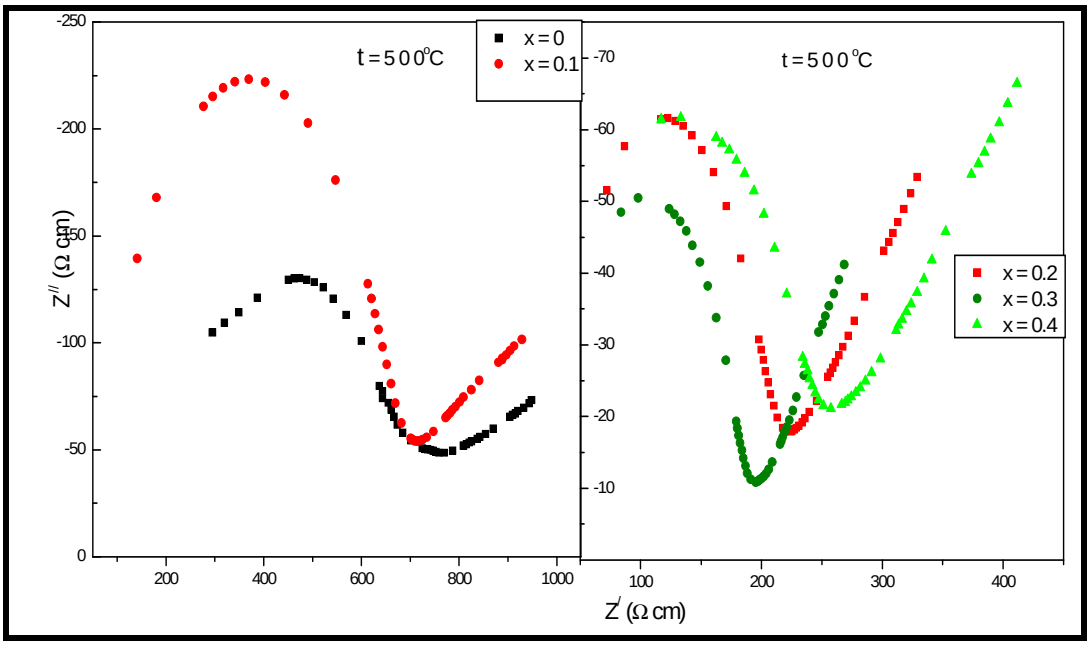

Fig. 3.5(c): Cole-Cole plot of $Bi_{4-x}Li_xV_2O_{11-\delta}$ ($0 \leq x \leq 0.4$) at 500°C.

The Arrhenius plots depicting the conductivity behaviour of $Bi_{4-x}Li_xV_2O_{11-\delta}$ ($0 \leq x \leq 0.4$) series of compounds has been shown in the **Fig. 3.6**. The conductivity plots for the compound with compositions x=0 and x=0.1 show three linear regions associated with the three principal polymorphs α, β and γ. On the other hand, β polymorph appears to be partially stabilized with compositions x=0.2 to x=0.4 and exhibits less linearity in the conductivity plot. This behaviour of the system agrees well with the findings of DSC measurements. It has been observed that for the compositions x=0.2 – 0.4, there appears a noticeable increase in the slope of the conductivity curve around 470 °C. This change might be assumed as the initiation of transition to the γ-phase. One more noticeable feature in the conductivity plot is the appearance of peaks for lower level of substitutions (up to x=0.3) in the temperature range 400 °C to 500 °C with a trend of shifting towards the lower temperature region which is a general property of BIMEVOXes for lower level of substitutions **[30].** As shown in the **Fig.3.6**, the conductivity behaviour observed in the Arrhenius plots can usually be sorting out into three regions, (a) low temperature region (up to 380 °C), (b) intermediate temperature region (380 °C to 470 °C), and (c) high temperature region (above 500 °C). In low temperature range, the conductivity of the compounds with

compositions range x = 0.1 to 0.3 is higher than the undoped compound $Bi_4V_2O_{11}$, whereas the conductivity of the compositions x=0.4 is less than the parent compound.

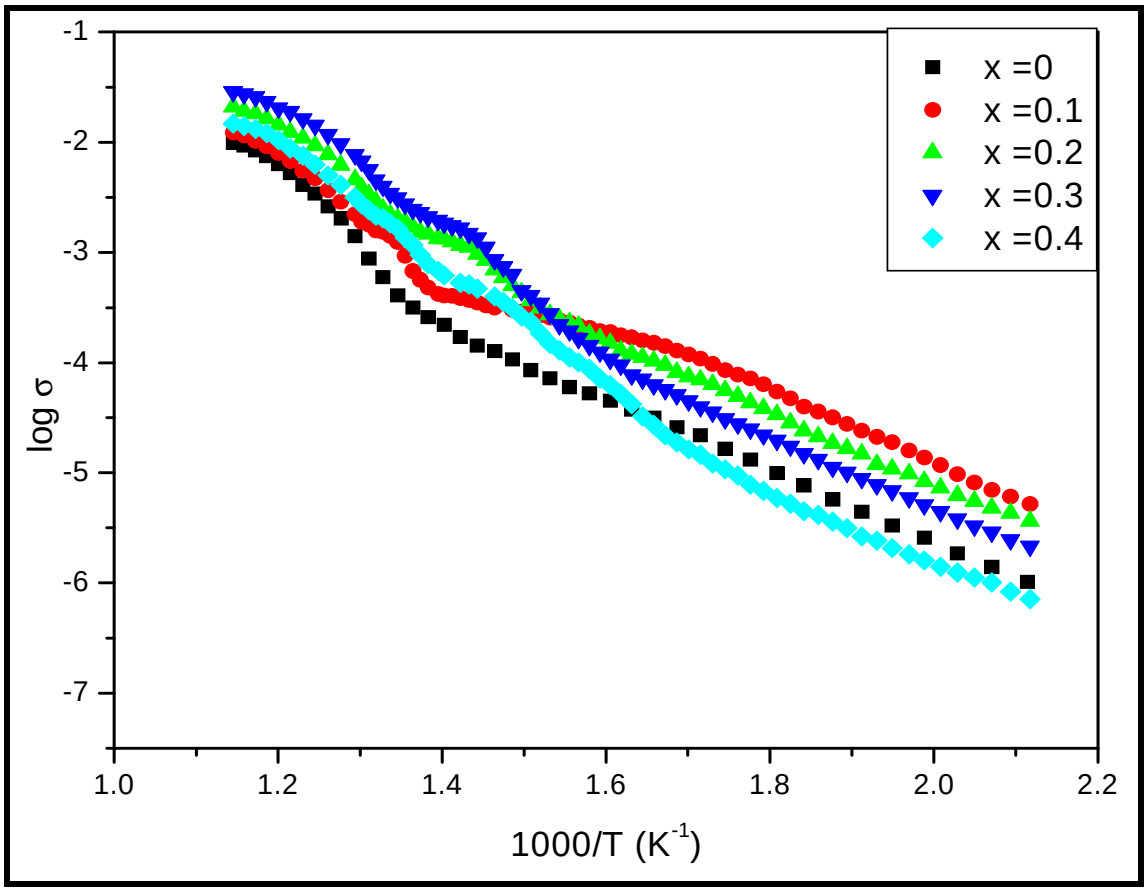

Fig. 3.6: Arrhenius plots of $Bi_{4-x}Li_xV_2O_{11-\delta}$ ($0 \leq x \leq 0.4$) series of compounds.

However, the conductivity of this specimen (x=0.4) is also found to be higher than the parent compound above 340 °C. In the low temperature regime, one could also note that there is gradual decrease in the conductivity with increasing doping concentration. The sintering temperature of the compound decreases with the increasing Li content (already tabulated in **chapter II**), thus, it might be expected that there would be an increase in grain boundary contribution with increasing dopant concentration and is evident from **Fig. 3.5(b)** which depicts the plot for grain boundary resistivity versus composition (x). The decrease in ionic conductivity with increasing Li-content is, therefore, result of increasing grain boundary contribution. Moreover, there is correlation between crystallite size and the low temperature

conductivity of these specimens. In the low temperature region, the conductivity decreases with the increasing crystallite size and the highest conductivity is observed for lowest crystallite size (for x = 0.1). For x > 0.1, there is a systematic decrease of conductivity with the increase of crystallite size. Such type of ionic conductivity dependence on crystallite size was also reported for other BIMEVOXes **[31-32]**. In the intermediate temperature range between 380 $^{\circ}$C to 470 $^{\circ}$C, the conductivities of all the doped specimens are found to be remarkably higher than the undoped compound. In this range of temperature, the lowest and highest conductivities are observed for the compounds with compositions x = 0.1 and x = 0.3, respectively. In the intermediate range of temperature, the highest conductivity (1.6×10^{-3} S cm^{-1}) is obtained for x = 0.3 at 430 $^{\circ}$C which is one order higher than the parent compound. Above 500 $^{\circ}$C, all the doped compounds exhibit higher ionic conductivity than the undoped compound. In the higher temperature region also the highest and lowest conductivities are obtained for compositions x = 0.3 and x = 0.1 respectively. Thus the trend of conductivity remain unchanged in both the regions i.e., in intermediate as well as in high temperature region. The significant increase of ionic conductivity for the substituted phases as compared to the parent compound might be correlated with the increasing oxygen vacancies created by aliovalent substitution (Li^+) **[1, 33].** At lower level of substitution (x = 0.1), there exist lesser number of vacancies and hence exhibited lower conductivity. At higher temperatures, with the increase of substitution level more and more vacancies are generated. As a result, the conductivity gradually increases and reaches maximum for x = 0.3. On the other hand, the decrease of ionic conductivity for x=0.4 composition with increasing oxygen vacancy (Li content) can be explained as a result of defect pair formation **[4].**

3.4 Conclusion

1. X-ray diffraction and DSC measurements on the samples reveal partial suppression of β-polymorph in the substitution range $x \geq 0.2$ at room temperature.

2. The SEM micrographs show uniformly distributed well grown grains with good grain to grain connectivity. The interwoven wavy network observed in the samples signifies ferroelectricity.

3. DSC profiles for both the parent as well as the doped compound show noticeable hysteresis behaviour.

4. In the intermediate and high temperature region, the conductivity of all the doped specimens is higher than the parent compound.

5. The highest conductivity (1.6×10^{-3} S cm^{-1}) with respect to the parent compound is obtained for x = 0.3 at 430 $^{\circ}$C.

6. The higher ionic conductivity observed in doped samples with respect to the parent compound can be correlated with the creation of excess oxygen ion vacancies generated by aliovalent substitution.

References:

[1] J. Yam, M. Greenblatt, Solid State Ionics **81** (1995) 225-233.

[2] F. Krok, I. Abrahams, M. Malys, W. Bogusz, J. R. Dygas, J.A.G. Nelstrop, A.J. Bush, Solid State Ionics **136-137** (2000) 119-125.

[3] S. Beg, A. Al-Alas, N. A. S. Al-Areqi, Radiat. Eff. Defects. Solid **165** (2010) 894–906.

[4] C. K. Lee, A. R. West, Solid State Ionics **86-88** (1996) 235-239.

[5] S. Beg, N. A. S. Al-Areqi, S. Haneef, Solid State Ionics **179** (2008) 2260- 2264.

[6] I. Abrahams, F. Krok, Solid State Ionics **157** (2003) 139 –145.

[7] C. K. Lee, G. C. Lim, A. R.West, J. Mater. Chem. **4** (1994) 1441-1444.

[8] J. Sut, L. Bora, A. Pandey, J. Solid State Electrochem. (communicated)

[9] Y. Taninouchi, T. Uda, T. Ichitsubo, Y. Awakura, E. Matsubara, Solid State Ionics **181** (2010) 719–723

[10] V. Sharma, A. K. Shukla, J. Gopalakrishnan, Solid State Ionics **58** (1992) 359-362.

[11] B. Vaidhyanathan, K. Balaji, K. J. Rao, Chem. Mater. **10** (1998) 3400-3404.

[12] J. Sut, L. Bora, A. Pandey, IJIRD **1-7** (2012) 181-185

[13] E. Wu, POWD, an interactive powder diffraction data interpretation and indexing program, version 2.5, School of Physical Sciences, Finders University of South Australia, Bedford Park, Australia.

[14] R. Kant, K. Sing, O. P. Pandey, Ionic **15** (2009) 567-570.

[15] S. N. Achary, M. D Mathews, S. J Patwe, A. K Tyagi, J. Mater. Sci. Lett. **18** (1999) 355.

[16] C .K. lee, C. S. Ong, Solid State Ionics **117** (1999) 301-310.

[17] R. Ahlawat, P. Aghamkar, Acta Physica Polonica A**126** (2014) 737.

.[18] S. Beg, A. Al-Alas, N. A. S. Al-Areqi, Radiation Effects & Defects in Solids **165**, (2010) 894–906

[19] S. Beg, S. Hafeez, N. A. S. Al-Areqi, Phase Transitions **83**, No. 3, (2010), 169–181.

[20] M. Alga, A. Ammar, R. Essalim, B. Tanouti, F. Mauvy, R. Decourt, Solid State Sci. **7** (2005) 1173.

[21] H. M. Zaki, S. F. Mansour, J. Phys. Chem. Solids **67** (2006) 1643.

[22] C. Pirovano, M. C. Steil, E. Capoen, G. Nowogrocki, R. N. Vannier, Solid State Ionics **176** (2005) 2079-2083.

[23] B. Jaffe, W. R. Cooke and H. Jaffe, Piezoelectric Ceramics, Academic press, 1971.

[24] Y. Xu, Ferroelectric Materials and Their Applications, North Holloand, 1991.

[25] K. V. R Prasad, G. N Subbanna, K. B. R. Varma, Bull. Mater. Sci. **17**, No. 3 (1994) 299-306.

[26] E. A. Fortalnova, V. V. Murasheva,, M. G. Safronenko,, N. U. Venskovskii,G. M. Kaleva, S. Yu. Stefanovich, E. D. Politova, Bulletin of the Russian Academy of Sciences: Physics, **72** No. 8 **(**2008) 1094–1097

[27] K. Shantha, K. B. R. Varma, Solid State Ionics **99** (1997) 225-231

[28] R. Kant, K. Sing, O. P. Pandey, Ceramics International **35** (2009) 221–227.

[29] R. N. Vannier, G. Mairesse, F. Abraham, G. Nowogrocki, Solid State Ionics **80** (1995) 11-17.

[30] Yu. V. Emel'yanova, E. N. Tsygankova, S. A. Petrova, E. S. Buyanova, V. M. Zhukovskii, Russ. J. Electrochem. **43** (2007) 737–741.

[31] C.H. Hervoches, M.C. Steil, R. Muccillo, Solid State Sciences **6** (2004) 173–177

[32] M.C. Steil, J. Fouletier, P. Labrune, J. Eur. Ceram. Soc. **19** (1999) 815.

[33] R. Kant, K. Sing, O. P. Pandey, Int. J. Hydrogen Energy **33** (2008) 455-462